ASME Journal of Thermal Science and Engineering Applications
Online journal at:
https://asmedigitalcollection.asme.org/thermalscienceapplication

Experimental Validation of Reynolds–Prandtl Scaling for Confined Gas Jet Impingement Heat Transfer

Alexandros Peteinaris
Thermo-Fluids and Interfaces Lab,
Faculty of Aerospace Engineering,
Technion–Israel Institute of Technology,
Haifa 3200003, Israel
e-mail: alexandrosp@campus.technion.ac.il

Acar Çelik
Turbomachinery and Heat Transfer Laboratory,
Faculty of Aerospace Engineering,
Technion–Israel Institute of Technology,
Haifa 3200003, Israel
e-mail: acar.celik@campus.technion.ac.il

Beni Cukurel[1]
Fellow ASME
Turbomachinery and Heat Transfer Laboratory
, Faculty of Aerospace Engineering,
Technion–Israel Institute of Technology,
Haifa 3200003, Israel
e-mail: beni@cukurel.org

Alexandros Terzis[1]
Thermo-Fluids and Interfaces Lab,
Faculty of Aerospace Engineering,
Technion–Israel Institute of Technology,
Haifa 3200003, Israel
e-mail: aterzis@technion.ac.il

The influence of gas transport properties on jet impingement heat transfer is commonly represented through a power law Prandtl number dependence, $Nu \propto Pr^n$, but experimental evidence for gas-to-gas sensitivity in strongly confined geometries remains limited. In the present work, heat transfer from a single, fully confined impinging jet with a single exit is investigated experimentally for five working gases (dry air, N_2, Ar, CO_2, and He) at matched jet Reynolds numbers, $Re_D \approx 15{,}000$–$30{,}000$, and a fixed jet-to-target spacing of $H/D = 1$. Spatially resolved heat transfer coefficients are obtained using transient liquid crystal thermography coupled with a one-dimensional transient conduction model based on Duhamel superposition. The driving temperature of the heat transfer experiment at the impingement surface is reconstructed from thermocouple measurements using a two-timescale step model with thermocouple response correction, ensuring consistent thermal boundary conditions across gases. After Reynolds normalization, air, N_2, Ar, and CO_2 show similar normalized heat transfer distributions, and a common Prandtl scaling collapses the stagnation and wall-jet regions. Helium remains an outlier despite Reynolds–Prandtl normalization, with a more compact footprint and steeper radial decay. A Brinkman number analysis indicates increased sensitivity of Helium to viscous dissipation and recovery temperature effects, due to the higher jet velocities required for Reynolds matching; a Brinkman-based rescaling improves the collapse. Overall, the results show that modest gas property variations can measurably alter confined-impingement heat transfer distributions, and that Reynolds–Prandtl scaling alone is insufficient for low-density gases under matched Reynolds conditions. [DOI: 10.1115/1.4071562]

Keywords: confined jet impingement, gas transport properties, heat transfer, liquid crystal thermography, electronic cooling, experimental techniques, experimental/measurement techniques, forced convection, gas turbine heat transfer, jets, wakes, and impingement cooling, thermophysical properties

1 Introduction

Double-wall turbine blade cooling architectures employ a thin outer wall backed by an inner structure that forms a network of internal cooling passages, bringing the coolant closer to the external surface [1–3]. In such confined cavities, the coolant is typically supplied in the form of impingement jets, and all internal surfaces contribute to cooling [4–6]. Consequently, the local heat transfer is strongly influenced by geometric confinement and cavity crossflow associated with spent-flow evacuation [7,8]. In addition, the small jet-to-target spacing can alter both the magnitude and the spatial distribution of heat transfer coefficients relative to unconfined impinging jets [9–11].

A substantial body of work has focused on how confined jet impingement heat transfer responds to geometric and flow management parameters, including sidewall proximity [12], confinement size dependence [13], impingement hole staggering [14], rotation [15,16], surface curvature [17,18], and design variables such as hole number and layout [19,20], crossflow mitigation via channel divergence or crossflow diverters [21,22], and variations in jet diameter and pitch [23–25].

In addition to turbine cooling, confined impingement configurations appear in electronics and optical/laser thermal management, where enclosure effects are inherent. In such systems, reliable similarity-based scaling across working gases is valuable for transferring design data between test conditions and operating environments. Indeed, jet impingement heat transfer is sensitive to working fluid transport properties through their control of momentum and thermal diffusion, commonly characterized by the Prandtl number, $Pr = \nu/\alpha$. Accordingly, heat transfer correlations prescribe a power law dependence of the Nusselt number, Nu, on Pr:

[1]Corresponding authors.
Manuscript received February 2, 2026; final manuscript received March 24, 2026; published online June 10, 2026. Assoc. Editor: Jae Su Kwak.

Copyright © 2026 by ASME

$Nu \propto Pr^n$. Because Pr governs the thermal-to-hydrodynamic boundary layer thickness ratio, it can, in principle, alter both local and area-averaged heat transfer, even when the momentum field is matched at a fixed Reynolds number [26]. This is particularly relevant in confined impingement cavities, where wall proximity constrains the near-wall flow development and may enhance the sensitivity of local heat transfer even to modest variations in Pr. Existing gas-based impingement correlations at low jet-to-wall spacing [5,27], however, represent Prandtl number effects using a fixed exponent (e.g., $Nu \propto Pr^{1/3}$), rather than explicitly quantifying Prandtl-number sensitivity across gases and confinement levels.

Despite its importance, Prandtl number effects in impingement heat transfer have largely been inferred from datasets spanning broad ranges of working fluids and configurations. For example, studies on confined and submerged geometries report Pr scalings ranging from 0.215 to 0.452 for the stagnation point and area-averaged heat transfer, respectively [26,28]. Such exponents are typically extracted by combining liquids and gases with Prandtl numbers differing by orders of magnitude (e.g., $Pr \in [0.68, 450]$) [26,28–32]. Across such wide Pr ranges, a single global fit is unlikely to remain uniformly accurate because the inferred exponent effectively averages over distinct transport regimes and fluid classes rather than capturing sensitivity within a narrower subset of conditions.

For gas-phase jet impingement, the Prandtl number of common gases (air, N_2, Ar, CO_2, He) span only a narrow range (typically 0.66–0.76), and much of the experimental evidence motivating Pr effects for gases other than air originates from submerged or semi-confined jets [29,33]. In these configurations, entrainment and molecular diffusion can promote local mixing between the jet and the surrounding laboratory air, leading to spatially varying composition and ill-defined effective properties and thermal boundary conditions. Complementary computational fluid dynamics studies indicate that Pr sensitivity may vary locally (e.g., between stagnation and wall-jet regions) [26,34]. However, these predictions depend on turbulence-model assumptions that can be more consequential in confined cavities where shear-layer development and jet–wall interactions are tightly coupled.

To isolate transport property effects in confined gas jet impingement, a cross-gas comparison at matched Reynolds number is required. Holding Re fixed preserves viscous scaling while allowing the relative rates of momentum and heat diffusion (and associated property ratios) to vary. This approach directly tests whether the modest variation in Pr yields measurable changes in local heat transfer distributions.

This study experimentally investigates gas jet impingement heat transfer in an enclosed, single-outlet confined configuration using air, nitrogen (N_2), argon (Ar), carbon dioxide (CO_2), and helium (He) at matched Reynolds numbers spanning 15,000–30,000. Helium was included as a low-density, high thermal conductivity gas to provide a strong transport property contrast and to test the limits of classical Reynolds–Prandtl similarity under matched Reynolds number. Local heat transfer coefficient distributions are obtained with high spatial resolution using transient liquid crystal thermography and a transient conduction model. The time-resolved driving temperature (i.e., the mainstream temperature driving the transient experiment) at the test section, $T_\infty(t)$, is reconstructed from thermocouple measurements using a two-timescale step model and thermocouple thermal response correction. The reconstructed inlet-temperature history is then imposed as the model input, ensuring consistent thermal boundary conditions across gases. The resulting datasets quantify how gas-to-gas variations in transport properties map onto local Nusselt number distributions.

2 Experimental Setup

2.1 Test Rig. An experimental setup was designed and built, depicted in Fig. 1. Compressed gas (dry air, N_2, CO_2, Ar, or He; gas properties at ambient conditions are listed in Table 1 [35]) is regulated by a mass-flow controller and enters the test section through a bellmouth and honeycomb flow straightener. Two resistive heater meshes generate a step change in the mainstream temperature via Joule heating. The resulting temperature history is monitored by an exposed-junction K-type thermocouple (bead diameter 0.18 mm). The small bead size was selected to minimize thermal inertia and provide a fast dynamic response needed for the reconstruction of the transient driving temperature history. The heated flow passes through a circular orifice plate ($D = 15$ mm) to form an impinging jet that impacts a thermochromic liquid crystal (TLC)-coated target plate in a confined chamber. The spent flow is forced to exit in a single direction and is discharged to ambient (Sec. 2.2).

A key requirement of a transient heat transfer experiment is a rapid change in the mainstream (or driving) temperature, while the optical response of a liquid crystal coating is recorded in time. The temperature step is generated via Joule heating using two resistive woven meshes (stainless steel 304) and measured with a K-type thermocouple with an exposed junction (bead diameter 0.18 mm) located on the duct centerline in the approach duct, 10 cm downstream of the heater, and 10 cm upstream of the

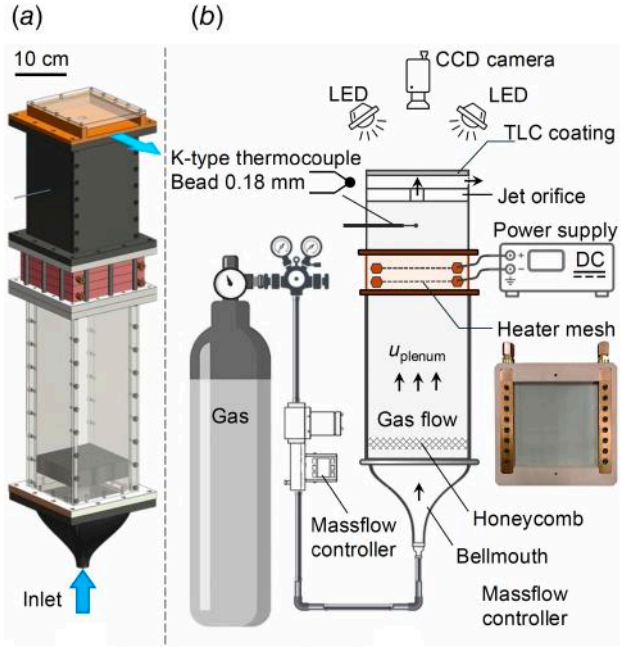

Fig. 1 (*a*) CAD rendering of the experimental setup. (*b*) Schematic of gas delivery and measurement system. Working gas is supplied from high-pressure cylinders and routed to a square-duct housing a heater-mesh assembly. Downstream of the heater, the flow passes through an orifice-plate jet and discharges into a confined impingement chamber, where the spent jet exits in a single direction. The surface temperature is recorded through a transparent acrylic target (back-side imaging) using a CCD camera under uniform illumination.

Table 1 Gas thermophysical properties at 20 °C, 1 atm

Gas	Pr	μ ($\times 10^{-5}$) (Pa s)	c_p (kJ/kg/K)	k (W/m/K)
Dry air	0.710	1.81	1.005	0.0250
N_2	0.716	1.76	1.041	0.0256
Ar	0.660	2.23	0.520	0.0176
CO_2	0.760	1.47	0.844	0.0166
He	0.670	1.96	5.193	0.151

orifice plate. Each mesh has a wire diameter of 25 μm and an aperture of 38 μm (open area: 35%) and spans the full plenum cross section ($120 \times 120\,\text{mm}^2$). Electrical power is supplied by a 15 kW DC power supply (EA-PS 10200-210 3U, Elektro-Automatik GmbH). The transient response of liquid crystals is recorded with a CCD camera (2592×2048, U3-3180CP, IDS Imaging Development Systems GmbH) viewing the target through the transparent acrylic substrate. The camera is mounted perpendicular to the target surface and synchronized with the heating event. The imaging magnification yields a spatial calibration of approximately 7.7 pixels/mm. Uniform illumination is provided by two high-intensity white LED sources (MultiLED QX, GSVitec), mounted symmetrically on either side of the confined chamber.

2.2 Confined Impingement Jet Chamber. Figure 2 shows a schematic of the confined impingement box. Confinement is used to reduce entrainment of laboratory air and limit mixing of the tested gas with the surroundings, thereby maintaining a well-defined working fluid composition within the measurement region. The test section is a shallow cavity bounded by a jet plate and a target plate. The impinging jet is formed by a circular orifice of diameter $D = 15$ mm in the jet plate and impacts the target plate normally, with a fixed jet-to-target spacing of $H/D = 1$. In the streamwise direction, the distance from the left lateral wall to the exit is $x/D = 10$. The orifice centerline is located at $x_{\text{jet}}/D = 4$ from the left wall, i.e., $6D$ upstream of the exit. In the spanwise direction, the half-width from the symmetry plane to the sidewall is $y/D = 4$.

The target plate is coated with TLCs for spatially resolved surface temperature measurements and is fabricated from transparent acrylic to enable optical access from the back side. A schematic of the coating stack is shown in Fig. 3. The thickness of the plate (12 mm), together with the low thermal conductivity of acrylic ($k_w = 0.18$ W/m/K), supports the one-dimensional, semi-infinite approximation over the transient time window used for data reduction [36] (see Sec. 3).

For each experiment, the jet Reynolds number based on the orifice diameter D is computed as follows:

$$\text{Re}_D = \frac{\rho U D}{\mu(T_{\text{jet}})} = \frac{4\dot{m}}{\pi D\,\mu(T_{\text{jet}})} \tag{1}$$

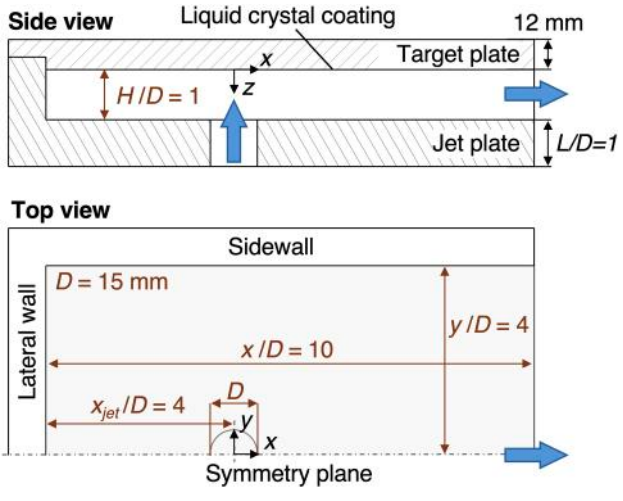

Fig. 2 Confined impingement-jet chamber geometry. A circular orifice ($D = 15$ mm) forms the impinging jet, which impacts the TLC-coated target plate at $H/D = 1$. The spent flow is forced to exit in a single direction; the downstream exit is located at $x/D = 6$, and the lateral clearance to the sidewall is $y/D = 4$ (top view).

where $\dot{m} = \rho U(\pi D^2/4)$ is the mass flowrate prescribed by the mass-flow controller (Alicat Scientific, model MCR-3000). The dynamic viscosity μ of the working gas is evaluated at the hot operating condition using an estimated jet exit static temperature, T_{jet}. This static temperature is obtained from the measured plenum (stagnation) temperature, assuming adiabatic discharge through the orifice. The exit velocity is inferred from the imposed mass flowrate using an effective discharge area C_dA, where C_d is evaluated from a published correlation [37], and the back pressure is assumed to be ambient. For all gases, the heat transfer experiments were conducted at matched jet Reynolds numbers, $\text{Re}_D = 15000$, 20000, 25000, and 30000, so that differences in the measured heat transfer primarily reflect gas property effects rather than changes in viscous scaling. The operating conditions for each gas are presented in Table 2. Consequently, the required mass flowrate (and thus the jet exit velocity) varies among gases to satisfy the matched Re_D.

3 Measurement Technique

3.1 Heat Transfer Model and Duhamel Superposition. Transient liquid crystal thermography infers the local heat transfer coefficient h from the transient temperature response of a wall-coated system following a change in the mainstream (driving) temperature $T_\infty(t)$. The thermal response is modeled as one-dimensional transient conduction normal to the surface, with $z = 0$ at the flow-exposed surface, as shown in Fig. 3. If the thermal conductivity of the wall is sufficiently small, in this case, $k_w = 0.18$ W m^{-1} K^{-1}, lateral conduction can be neglected such that $T_w = T_w(z, t)$ [36]. Assuming constant properties for the wall and a semi-infinite body, the governing equation, together with the initial and boundary conditions, is given as follows:

$$\frac{\partial T_w}{\partial t} = \alpha_w \frac{\partial^2 T_w}{\partial z^2}, \quad \alpha_w = \frac{k_w}{\rho_w c_{p,w}} \tag{2a}$$

$$T_w(z, 0) = T_{w,0}, \quad z \in [0, \infty) \tag{2b}$$

$$-k_w \left.\frac{\partial T_w}{\partial z}\right|_{z=0} = h[T_\infty(t) - T_s(t)], \quad T_s(t) \equiv T_w(0, t) \tag{2c}$$

$$\lim_{z\to\infty} T_w(z, t) = T_{w,0}, \quad t > 0 \tag{2d}$$

where α_w, ρ_w, $c_{p,w}$, and k_w are the thermal diffusivity, density, specific heat, and thermal conductivity of the wall, respectively. At $t = 0$, the wall is assumed to be in thermal equilibrium with the mainstream, such that

$$T_{w,0} = T_{\infty,0} \tag{3}$$

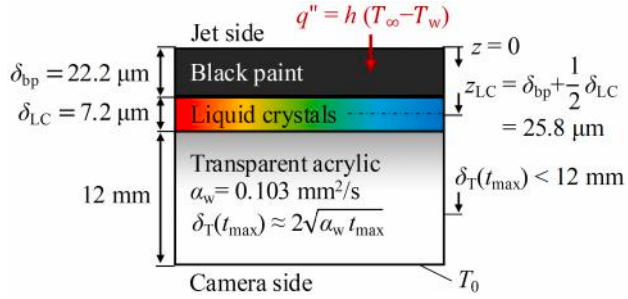

Fig. 3 TLC coating stack and effective indication depth. The TLC temperature is assigned to the mid-plane of the liquid crystal layer located at $z_{\text{LC}} = 25.8 \pm 2.1\,\mu$m. The thickness of the black paint δ_{bp} and the liquid crystals δ_{LC} are, respectively, $22.2 \pm 2.0\,\mu$m and $7.2 \pm 1.5\,\mu$m.

Table 2 Operating conditions for each working gas

Gas	Re_D	ρ (kg/m^3)	u (m/s)	Ma	Ec
Air	15,338	1.050	19.9	0.054	0.0087
	20,409	1.063	25.9	0.071	0.0163
	25,481	1.072	31.9	0.088	0.0265
	30,553	1.078	37.9	0.105	0.0395
N_2	15,332	1.015	19.9	0.053	0.0085
	20,491	1.033	25.8	0.069	0.0161
	25,672	1.047	31.6	0.086	0.0259
	30,778	1.053	37.4	0.102	0.0387
Ar	15,318	1.360	20.0	0.057	0.0114
	20,353	1.386	25.7	0.074	0.0209
	25,446	1.408	31.2	0.090	0.0340
	30,584	1.435	36.2	0.106	0.0516
CO_2	15,545	1.535	11.8	0.041	0.0026
	20,408	1.543	15.4	0.054	0.0045
	25,655	1.576	18.6	0.065	0.0074
	30,741	1.591	21.9	0.077	0.0109
He	15,335	0.158	132.9	0.128	0.1837
	20,497	0.159	175.9	0.179	0.3544
	25,781	0.161	216.8	0.212	0.6305

Note: The gas density is evaluated at hot operating conditions (heater mesh energized) at an absolute pressure of 1 atm.

where $T_{\infty,0}$ is the initial mainstream temperature prior to transient.

The transient conduction problem defined by Eqs. (2a)–(2d) has a closed-form solution for an ideal step change in the mainstream temperature from $T_{\infty,0}$ to $T_{\infty,1}$:

$$\frac{T_w(z,t)-T_{\infty,0}}{T_{\infty,1}-T_{\infty,0}} = erfc\left(\frac{z}{2\sqrt{\alpha_w t}}\right) - \exp\left(\frac{hz}{k_w}+\frac{h^2\alpha_w t}{k_w^2}\right) erfc\left(\frac{z}{2\sqrt{\alpha_w t}}+\frac{h\sqrt{\alpha_w t}}{k_w}\right) \tag{4}$$

Here, $T_w(z,t)$ denotes the temperature within the wall, at depth z from the flow-exposed surface ($z=0$) and time t after the applied temperature step. In practice, however, the driving temperature $T_\infty(t)$ at the impingement location is not an ideal step because the heater-plenum-duct system has finite thermal inertia and the flow has a finite convective residence time. The temperature rise is thus distributed in space and time and reaches the target as a nonideal transient. Accordingly, Duhamel's superposition is used to compute the wall response by representing it as a continuum of infinitesimal temperature steps [38]. Let $\Phi(z,t;h)$ denote the nondimensional wall response to an ideal step change of $\Delta T_\infty = T_{\infty,1} - T_{\infty,0}$, i.e.,

$$\Phi(z,t;h) \equiv \frac{T_w^{step}(z,t)-T_{\infty,0}}{\Delta T_\infty}, \quad \Delta T_\infty = T_{\infty,1}-T_{\infty,0} \tag{5}$$

where $T_w^{step}(z,t)$ is given by Eq. (4). For a general driving temperature history $T_\infty(t)$, Duhamel's theorem yields

$$T_w(z,t) = T_{w,0} + \int_0^t \frac{dT_\infty(t')}{dt'}\,\Phi\big(z,t-t';h\big)\,dt' \tag{6}$$

Here, t' is an integration variable representing earlier times in the driving temperature history and $\Phi(z,t-t';h)$ is the ideal step response evaluated at the elapsed time $(t-t')$ since that infinitesimal change. Thus, Eq. (6) expresses $T_w(z,t)$ as the superposition of the wall responses to all prior incremental temperature steps over $0 \le t' \le t$.

3.2 Driving Temperature History $T_\infty(t)$ Reconstruction. The driving temperature required for the Duhamel analysis $T_\infty(t)$ is reconstructed from the thermocouple measurements using a parametric input-sensor model. Assuming a lumped-capacitance response for the exposed thermocouple bead, the measured temperature signal $T_m(t)$ is modeled as the output of a first-order lag driven by $T_\infty(t)$ [39]:

$$\tau_{tc}\frac{dT_m}{dt} + T_m = T_\infty(t) \tag{7}$$

where τ_{tc} is the thermocouple time constant, calculated from a lumped-capacitance estimate using a Nusselt number correlation for exposed beads [40]:

$$Nu_{tc} = -2.232\,\delta^{-0.546} + 2.847 + 0.379\,Re_{tc}^{0.573}\,Pr^{0.441} \tag{8}$$

Here, δ is the bead-to-wire diameter ratio, and all gas properties are evaluated at film conditions, $T_f = 0.5\big(T_{\infty,0}+T_{\infty,1}\big)$.

The unknown driving temperature history is then parameterized as a two-timescale nonideal step:

$$T_\infty(t) = \begin{cases} T_{\infty,0}, & t < t_0, \\ [t]T_{\infty,0} + \Delta T_\infty\big[1 \quad -\beta\, e^{-(t-t_0)/\tau_1} \quad -(1-\beta)\, e^{-(t-t_0)/\tau_2}\big] & t \ge t_0, \end{cases} \tag{9}$$

where $T_{\infty,0}$ and $T_{\infty,1}$ are the prestep and poststep plateaus obtained from time-averaged segments of the measured signal, t_0 is the step onset time, and τ_1, τ_2, and $\beta \in [0,1]$ describe the fast and slow components of the temperature rise. In particular, β represents the fraction of the step amplitude attributed to the fast mode, such that $\beta \to 1$ yields a nearly single-exponential rise with timescale τ_1, whereas $\beta \to 0$ emphasizes the slow component governed by τ_2.

For a candidate parameter set $\boldsymbol{\theta} = \{\tau_1, \tau_2, \beta, t_0\}$, the modeled thermocouple response $T_m^{model}(t)$ is obtained by numerically integrating Eq. (7) using the experimental sampling interval and the parameterized driving temperature given by Eq. (9). The parameters are estimated by nonlinear least-squares minimization of the residual between the measured and modeled signals over a fitting window spanning the transient, from the step onset t_0 to $t_{0.99}$:

$$\boldsymbol{\theta}^* = \arg\min_{\boldsymbol{\theta}} \sum_{i\,:\,t_i \in [t_0,\,t_{0.99}]} \big[T_m(t_i) - T_m^{model}(t_i;\boldsymbol{\theta})\big]^2 \tag{10}$$

Here, $t_{0.99}$ denotes the time at which the modeled driving temperature $T_\infty(t)$ reaches 99% of the total step magnitude. The reconstructed driving temperature used in the Duhamel analysis is then obtained from Eq. (9) using the optimal parameter set $\boldsymbol{\theta}^*$ from Eq. (10).

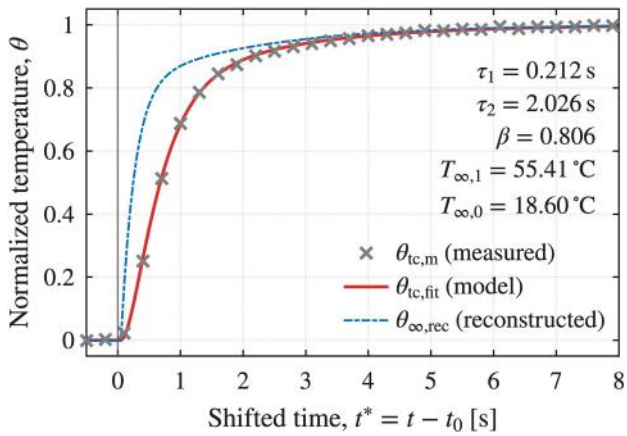

Fig. 4 Representative thermocouple step-response analysis used to reconstruct the driving temperature history for Duhamel superposition. The thermocouple signal, $\theta_{tc,m}$, is fitted with a two-timescale nonideal step input model (solid line), yielding the reconstructed driving temperature, $\theta_{\infty,rec}$ (dashed line). The inferred input parameters (τ_1, τ_2, β) and the prestep/poststep plateaus ($T_{\infty,0}$, $T_{\infty,1}$) are indicated.

Figure 4 shows a representative reconstruction in normalized form, i.e., $\theta(t) = (T(t) - T_{\infty,0})/(T_{\infty,1} - T_{\infty,0})$. The thermocouple signal $\theta_{\mathrm{tc,m}}$ is closely matched by the modeled response $\theta_{\mathrm{tc,fit}}$ over the entire transient. The inferred driving history $\theta_{\infty,\mathrm{rec}}$ rises more rapidly than the thermocouple output at early times, consistent with the finite sensor response and upstream mixing/transport effects that smear the apparent step. By construction, both the model output and reconstructed input asymptotically approach the same poststep plateau, ensuring consistency with the experimentally determined prestep and poststep temperatures $(T_{\infty,0}, T_{\infty,1})$. The fitted parameters (τ_1, τ_2, β) provide a compact description of the nonideal step shape. As intended, τ_1 captures the fast rise component, τ_2 captures the slower tail associated with thermal inertia and residence time dispersion, and β sets their relative weighting. For instance, $\beta = 0.8$ implies that about 80% of the step is realized through the fast mode (timescale τ_1), with the remaining ~20% contributed by the slow tail (timescale τ_2).

3.3 Thermochromic Liquid Crystal Indication Depth and Peak-Intensity Processing. The TLC signal corresponds to an effective measurement plane within the coating stack (see Fig. 3). Thus, the measured TLC temperature is denoted as $T_{\mathrm{LC}}(t) = T_{\mathrm{w}}(z_{\mathrm{LC}}, t)$. Because the TLC layer is sprayed beneath the black-paint overcoat, the optical signal does not correspond to the fluid–solid interface ($z = 0$). Therefore, the effective indication depth is taken as the mid-plane of the TLC layer, as shown in Fig. 3 [41,42]. For the present TLC coating, the black paint and the liquid crystal thicknesses are $\delta_{\mathrm{bp}} = 22.2 \pm 2.0\,\mu$m and $\delta_{\mathrm{LC}} = 7.2 \pm 1.5\,\mu$m (mean ± SD), respectively, measured using a coating-thickness gauge (Elcometer 456, nonferrous probe N) on a co-sprayed copper witness block. The TLC used here is a narrowband formulation (R31C1W, LCR Hallcrest). Under fixed illumination, the reflected intensity in each RGB channel exhibits a distinct peak over a narrow temperature interval. For each pixel, the green-channel intensity histories are processed to identify the peak intensity times t_{G}. This corresponds to the calibrated peak intensity temperature, $T_{\mathrm{G}} = 30.86\,^{\circ}$C, providing a temperature indicator at $z_{\mathrm{LC}} = 25.8\,\mu$m.

3.4 Determination of the Heat Transfer Coefficient. In data reduction, Eq. (6) is evaluated using a recovery-corrected driving temperature imposed at the test surface. Specifically, the time history reconstructed from the thermocouple analysis (Sec. 3.2) is converted to a pixel-resolved adiabatic wall (recovery) temperature field, T_{aw}, which is used as the driving input in the Duhamel superposition:

$$T_{\mathrm{aw}} = T_{g,\mathrm{rec}}(t) + (r - 1)\, T_d \tag{11}$$

Here, $T_{g,\mathrm{rec}}(t)$ is the reconstructed bulk gas temperature history, r is a recovery factor map prescribed from literature sources [43–45] as a function of r/D and mapped to the target plate, and T_d is the dynamic temperature estimated from the average jet velocity as $U^2/(2c_p)$ under low Mach number conditions.

For data sampled discretely at times t_n, Eq. (6) is evaluated in incremental form as follows:

$$T_{\mathrm{w}}(z, t_n) = T_{\mathrm{w},0} + \sum_{i=1}^{n} \Delta T_{\mathrm{aw},i}\, \Phi(z, t_n - t_i; h), \qquad \Delta T_{\mathrm{aw},i} \equiv T_{\mathrm{aw}}(t_i) - T_{\mathrm{aw}}(t_{i-1}) \tag{12}$$

For a given heat transfer coefficient h, Eq. (12) provides the model prediction $T_{\mathrm{w}}(z_{\mathrm{LC}}, t_n; h)$ at the TLC indication depth. In the present study, the heat transfer coefficient is determined using the green-channel peak intensity indicator only. Specifically, for each pixel, h is obtained by matching the modeled wall temperature at the TLC indication depth to the calibrated green peak temperature T_{G} at the corresponding peak time t_{G}, i.e.,

$$T_{\mathrm{w}}(z_{\mathrm{LC}}, t_{\mathrm{G}}; h) = T_{\mathrm{G}} \tag{13}$$

This scalar equation is solved independently for each pixel using a one-dimensional nonlinear solver. A representative example of the full-field heat transfer coefficient evaluation, together with details of the uncertainty analysis are provided in Appendix A. Thermophysical properties used to evaluate the dimensionless groups Nu, Pr, and St are taken at the jet exit static temperature T_{jet} to ensure consistency across all gases. The temperature dependence of the main thermophysical properties of the gases is discussed in Appendix B.

4 Results and Discussion

4.1 Symmetry Verification. To verify the symmetry of the heat transfer distribution, a full-field contour for a representative case (air, $Re_D = 25\,000$) is provided in Fig. 12(*a*) in Appendix A. The distribution exhibits near-axisymmetric behavior about the spanwise centerline ($y/D = 0$). Symmetry was quantified by comparing the mirrored upper and lower halves of the surface, yielding a mean absolute deviation below ~6% across all cases, with a maximum of ~11%. Therefore, the heat transfer maps are mirrored and averaged about $y/D = 0$ to reduce random measurement noise.

4.2 Normalized Stanton Number Maps. Figure 5 shows normalized contours of the Stanton number at $\mathrm{Re}_D \approx 25\,000$ for all tested gases (air, N_2, Ar, CO_2, and He). The contours are normalized by the stagnation point Stanton number, $\mathrm{St}_{\mathrm{sp}}$, in order to remove differences in absolute magnitude and to enable a direct comparison of contour shape across gases. For all gases, a distinct maximum is observed at the stagnation point, followed by a monotonic decay in both the radial and streamwise directions, indicating a well-defined impingement region (Figs. 5(*a*)–5(*e*)). The normalized isolines form approximately concentric contours around the stagnation region, reflecting a largely axisymmetric redistribution of the impingement footprint under confined conditions.

Air and N_2 exhibit nearly identical normalized contour patterns (Figs. 5(*a*) and 5(*b*)). The $\mathrm{St}/\mathrm{St}_{\mathrm{sp}} = 0.6$, 0.4, and 0.3 isolines occur at comparable radial locations, yielding similar footprint size and decay rates. As expected, a mild asymmetry is observed on the upstream confinement side. As the wall at $x/D \approx -4$ is approached, the outer isolines are slightly compressed and locally displaced toward positive x/D, indicating constrained lateral spreading of the wall jet due to geometric confinement. The close overlap between air and N_2 provides a consistent baseline reference for assessing gas-dependent effects in the remaining cases.

Argon and CO_2 display systematically broader normalized heat transfer footprints (Figs. 5(*c*) and 5(*d*)). For these gases, the outer isolines—in particular $\mathrm{St}/\mathrm{St}_{\mathrm{sp}} = 0.4$ and 0.3—extend farther from the stagnation point in both the radial and streamwise directions, indicating a slower spatial decay of St along the developing wall jet. Among the gases, CO_2 exhibits the most extended footprint, with the largest enclosed area for the $\mathrm{St}/\mathrm{St}_{\mathrm{sp}} = 0.3$ isoline, consistent with reduced thermal diffusivity and altered transport in the confined wall-jet region.

Helium exhibits a markedly different normalized distribution (Fig. 5(*e*)). The high-$\mathrm{St}/\mathrm{St}_{\mathrm{sp}}$ core is strongly localized near the stagnation point, with the $\mathrm{St}/\mathrm{St}_{\mathrm{sp}} = 0.6$ isoline contracting toward the jet axis and a rapid decay beyond $y/D \approx 1$. Although helium yields substantially higher absolute stagnation point heat transfer coefficients (reported in-panel), normalization reveals that its relative heat transfer field is more tightly confined than those of air, N_2, Ar, and CO_2.

Overall, the normalized Stanton number contours demonstrate that, at matched Reynolds number, the extent, shape, and decay of the impingement heat transfer footprint depend strongly on

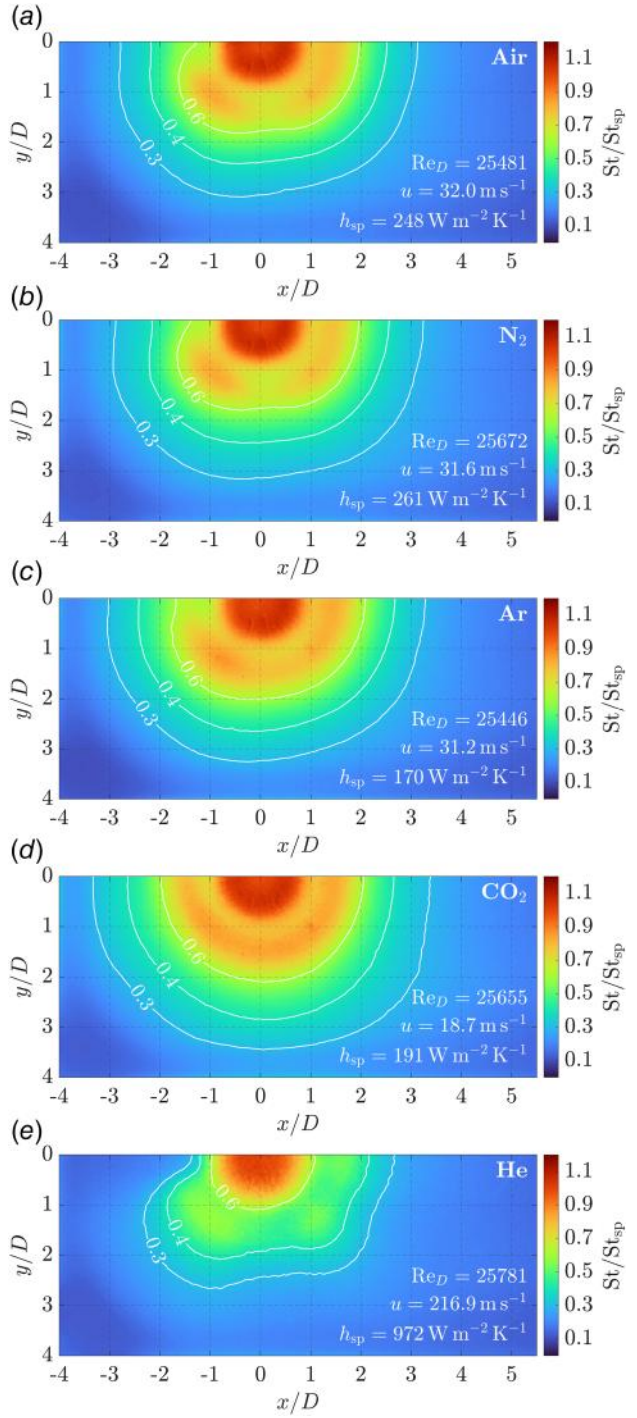

Fig. 5 Normalized surface contours of Stanton number, $\mathrm{St}/\mathrm{St_{sp}}$ at $\mathrm{Re_D} = 25\,000$ for all gases. h_{sp} denotes the stagnation point heat transfer coefficient.

gas properties beyond Reynolds number alone. Differences in transport characteristics manifest as systematic variations in isoline spreading and footprint size, even when absolute heat transfer levels are scaled out.

4.3 Reynolds-Normalized Nusselt Number Distributions. Figure 6 shows centerline ($y/D = 0$) Nusselt number distributions normalized by a Reynolds number power law with exponent m. This Reynolds-only normalization is applied to quantify and remove residual Reynolds number sensitivity before introducing any Prandtl number scaling. In practice, exact Reynolds number matching across gases is not attainable due to differences in density, viscosity, flow-control constraints, and finite uncertainties in mass flow and property estimation. As a result, even modest Reynolds mismatches can bias inter-gas comparisons if left uncorrected. Accordingly, m is identified independently for each gas as the value that provides the best collapse of data acquired over $\mathrm{Re}_D = 15{,}000 - 30{,}000$. For the present data, the best collapse is obtained with $m = 0.7$ for all gases, which is consistent with Reynolds exponents reported for confined single-jet impingement [46] and for multiple jet arrays, $m = 0.72$ [27].

For air and N_2, normalization with $m = 0.7$ yields near-complete collapse across the full centerline profile, from the stagnation region through the developing wall jet, consistent with their similar transport properties. Argon exhibits a comparably strong collapse, with only minor scatter near the secondary peak location ($x/D \approx -1.5$). CO_2 shows slightly greater dispersion in the near-stagnation region but collapses well both upstream and downstream, suggesting that Reynolds number effects remain the primary source of variation over most of the impingement surface. Helium, by contrast, shows only partial collapse across the tested Reynolds number range, with clear deviations for the highest Reynolds achieved for that case. Moreover, its normalized level and steeper upstream ($x/D < 0$) and downstream ($x/D > 0$) heat transfer decay remain different from the other gases, indicating a departure from this simple similarity scaling.

4.4 Prandtl-Normalized Nusselt Number Distributions. After identifying a Reynolds exponent $m = 0.7$ that collapses the Reynolds number dependence within each gas (Sec. 4.3), a second normalization is applied to isolate transport property effects associated with the Prandtl number, Pr. Specifically, the local Nusselt number is further normalized by $\mathrm{Pr}^{0.4}$, where an exponent 0.4 is adopted as a common Prandtl scaling for all gases. Note that in order to suppress residual scatter and emphasize systematic inter-gas trends, Reynolds-averaged distributions are formed for each gas by averaging the Reynolds-normalized data over the available Reynolds number cases presented in Fig. 6.

Figure 7 shows the Reynolds–Prandtl normalized centerline ($y/D = 0$) Nusselt number distributions. For air, N_2, Ar, and CO_2, the normalization produces a strong collapse over the stagnation region and the downstream wall-jet region ($x/D > 0$), indicating that a single Prandtl exponent captures the dominant gas-to-gas variation once Reynolds number effects are removed. In contrast, increased scatter is observed upstream of the stagnation point ($x/D < 0$). In this region, the flow is affected by confinement-induced recirculation near the lateral wall and by pressure gradients associated with stagnation and asymmetric evacuation toward the single exit. This is somewhat expected, considering that a Prandtl exponent of 0.4 conventionally stems from zero-pressure gradient flows. These features locally modify the near-wall velocity and turbulence structure, leading to departures from ideal similarity and deviating the collapse from the $\mathrm{Re}^{0.7}\mathrm{Pr}^{0.4}$ scaling. This is discussed further in Sec. 4.5.

Helium, on the other hand, exhibits a different response. Despite Reynolds and Prandtl normalization, its Nusselt number distribution remains systematically lower and decays more rapidly away from the stagnation point, making it a clear outlier relative to the heavier gases. This deviation indicates that additional mechanisms beyond classical Reynolds–Prandtl similarity influence helium heat transfer in the present confined configuration. In particular, although the highest Re case remains within the low Mach regime ($\mathrm{Ma} \approx 0.21$), the substantially higher jet velocities required to achieve matched Reynolds numbers with Helium may enhance the role of viscous dissipation and associated aerodynamic heating, increase sensitivity to the recovery/adiabatic wall temperature correction, and alter the effectiveness of turbulent heat flux transport under confinement.

The local Nusselt number ratios, $\mathrm{Nu}_D/(\mathrm{Re}_D^{0.7}\,\mathrm{Pr}^{0.4})$, are compared with experimental literature data for a fully confined

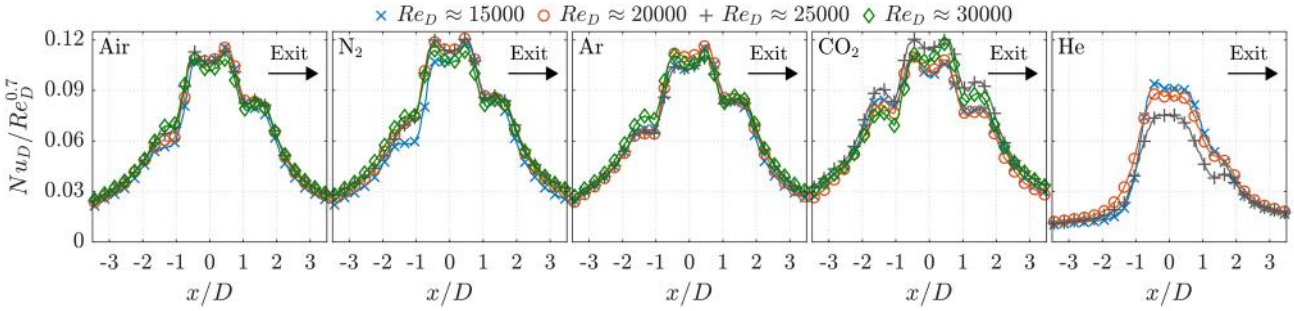

Fig. 6 Reynolds-normalized centerline ($y/D = 0$) Nusselt number distributions for different gases. Normalization by $Re_D^{0.7}$ collapses data across Reynolds numbers for each gas, isolating Prandtl number effects in both the stagnation and wall-jet regions.

impingement configuration [10], a fully developed jet issued from a pipe nozzle [47], and a multi-array arrangement with very large jet-to-jet spacing ($x/d = 10$) [48], providing a broader validation context for the present measurements. The present measurements collapse well onto the literature datasets in the stagnation region and in the location of the secondary heat transfer peak. Further downstream, small deviations appear as the wall jet develops. These differences are attributed to the confined geometry of the present setup, which induces lateral recirculation and streamwise pressure gradients associated with the asymmetric evacuation toward the single exit.

4.5 Local Mapping of Prandtl Number Exponent. To assess the influence of thermal diffusion on the local heat transfer distributions, an apparent Prandtl number exponent is estimated using a reduced gas dataset. The regression uses Ar, N_2, and CO_2. Air is excluded because its Prandtl number overlaps with that of N_2 while introducing potential systematic offsets (e.g., facility repeatability and run-to-run bias) that reduce resolvability over a narrow predictor span. Helium is also excluded because its distinct properties and flow/thermal behavior (very low density, high thermal conductivity, and altered recovery/viscous heating characteristics) violate the intent of a Pr-only perturbation, which can bias the fit through additional transport mechanisms (see Fig. 7).

Figure 8 shows a surface contour of the fitted response in the near-stagnation region ($-2 < x/D < 2$). Given the limited Pr span and the modest local goodness of fit, the fitted exponent is not interpreted as an absolute scaling constant. Instead, the map is used to diagnose relative Pr sensitivity through its spatial organization and dependency on local flow variations. Within the range tested, the near-stagnation region exhibits weak, fragmented apparent Pr-sensitivity, while the wall-jet region displays a more coherent structure, consistent with regime-dependent emergence of thermal diffusion effects downstream of stagnation. Notably, the best-fit exponent near the walls ($x/D = -2$ and $y/D = 2$) consistently converges to significantly larger values than that of the traditional 0.4 scaling, which is hypothesized to be associated, at least in part, with the complex secondary flow effects, but mostly driven by the local pressure gradient variations.

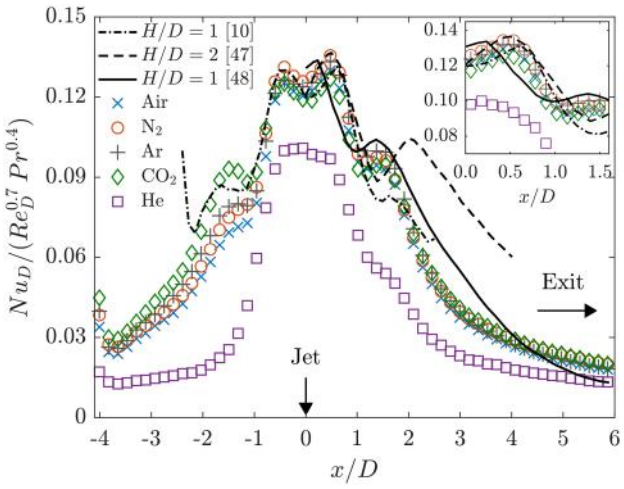

Fig. 7 Reynolds-averaged centerline Nusselt number ratios for all gases. Normalization with $Re_D^{0.7}$ and $Pr^{0.4}$ collapses air, N_2, Ar, and CO_2, while helium remains lower and decays more rapidly downstream, indicating that Pr^n scaling alone is insufficient over $Re_D = 15,000–30,000$.

4.6 Viscous Heating Effects and Brinkman Rescaling. The deviation of helium from the Reynolds–Prandtl similarity scaling suggests that additional mechanisms beyond classical momentum and thermal transport contribute to the measured heat transfer coefficients. In particular, the substantially higher jet velocities required to match Re_D with helium increase the relative importance of viscous dissipation, which can modify both the effective thermal driving and the inferred Nusselt number. To quantify this effect, the present data are analyzed using a viscous heating parameter based on the Brinkman number, and the local Nusselt number distributions are rescaled accordingly.

The Brinkman number is defined as the product of the Prandtl and Eckert numbers,

$$\mathrm{Br} = \mathrm{Pr}\,\mathrm{Ec} = \frac{\mu\, U_{\mathrm{jet}}^2}{k\,\Delta T} \tag{14}$$

where μ and k, are the dynamic viscosity and thermal conductivity of the working gas, respectively; U_{jet} is the mean jet exit velocity inferred from the imposed mass flowrate; and ΔT is the imposed

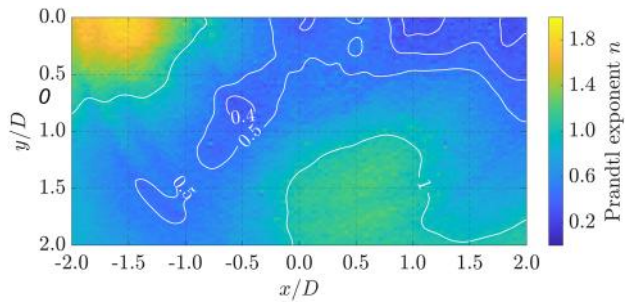

Fig. 8 Surface contour of the apparent Prandtl number sensitivity map in the stagnation region, obtained from pixelwise regressions using Ar, N_2, and CO_2. The fitted exponent is presented as a spatial diagnostic of Pr sensitivity rather than as an absolute scaling parameter due to the limited Prandtl number span and modest local goodness of fit.

thermal driving. At matched jet Reynolds number, $\mathrm{Re}_D = \rho U_{\mathrm{jet}} D/\mu$, substitution for U_{jet} yields

$$\mathrm{Br} = \frac{\mathrm{Re}_D^2}{D^2}\frac{\mu^3}{\Delta T}\frac{\rho^{-2}}{k} \tag{15}$$

demonstrating that, under matched Reynolds number conditions, the propensity for viscous heating increases strongly with decreasing gas density. Consequently, low-density gases such as Helium are inherently more susceptible to viscous dissipation and recovery temperature effects in high-velocity impingement flows, even when classical viscous scaling is preserved.

Figure 9 shows the Brinkman number as a function of the group $\rho^{-2}\mu^3(k\,\Delta T)^{-1}$. For air, N_2, Ar, and CO_2, Br remains below 0.1 across the investigated Reynolds number range, indicating that viscous heating effects are negligible. For helium ($\rho \approx 0.159$–$0.161\,\mathrm{kg/m^3}$), however, matching Re_D requires substantially higher jet velocities, which increases viscous dissipation and yields Brinkman numbers roughly an order of magnitude larger. Specifically, Br for helium is about 0.12, 0.24, and 0.42 at Reynolds numbers of about 15,000, 20,000, and 25,000, respectively.

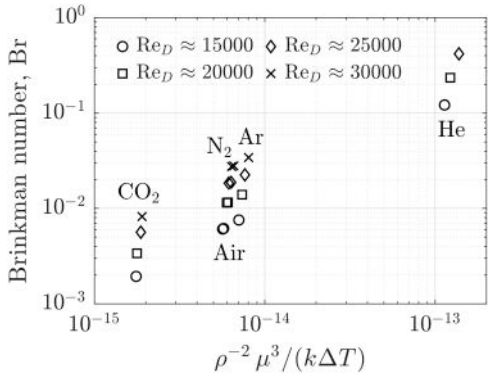

Fig. 9 Brinkman number Br plotted against the gas property group $\rho^{-2}\mu^3(k\,\Delta T)^{-1}$ ($\mathrm{m^2}$) for all working gases at matched Re_D. Helium exhibits substantially larger Br due to the higher jet velocities required to match Reynolds number at low density, implying increased sensitivity to viscous dissipation and recovery effects.

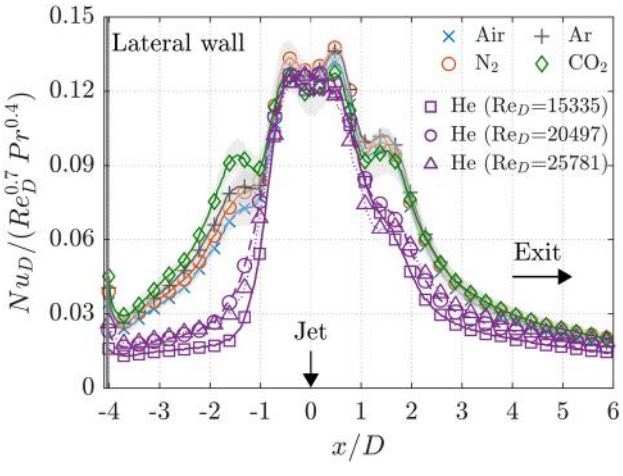

Fig. 10 Reynolds-averaged centerline Nusselt number distributions for air, N_2, Ar, CO_2, and He with a Brinkman-based viscous heating correction (Eq. (16)), normalized by $\mathrm{Pr}^{0.4}$. The correction is negligible for the heavier gases but increases the helium levels, indicating that viscous dissipation may contribute to the helium offset in the present confined configuration.

This suggests an enhanced sensitivity of the inferred heat transfer coefficients to viscous heating and recovery effects.

As a sensitivity test, the Nusselt number distributions are rescaled using a Brinkman correction of the form:

$$\mathrm{Nu_c} = \mathrm{Nu}\,(1 + C_{\mathrm{Br}}\,\mathrm{Br}) \tag{16}$$

where C_{Br} is an empirical coefficient that depends on the flow configuration. In the present study, no local velocity or wall-shear measurements were carried out to determine local C_{Br} variations or to resolve viscous dissipation within the wall-jet regions. Therefore, C_{Br} is taken as unity in order to assess the sensitivity of the Nusselt number to viscous heating effects in the stagnation point. The proposed correction should therefore be interpreted as a qualitative indicator of viscous heating relevance, rather than as a universal or spatially resolved correlation.

Figure 10 shows the Reynolds–Prandtl normalized centerline ($y/D = 0$) Nusselt number distributions before and after applying the Brinkman-based correction. After correction, He exhibits substantially improved collapse with the other gases, especially in the stagnation region and, to a lesser extent, in the developing wall-jet region toward the cavity exit, indicating that viscous heating effects account for a significant fraction of the observed deviation (see Fig. 7).

5 Area-Averaged Nusselt Number

Figure 11 shows the area-averaged Nusselt number, $\overline{\mathrm{Nu}}_D$, evaluated over the impingement region and rescaled using the Brinkman-based viscous dissipation correction. The data are shown as a function of the jet Reynolds number, Re_D, for all tested gases (air, N_2, Ar, CO_2, and He), together with representative literature correlations. It is emphasized that the cited correlations were originally developed for different geometries, such as multi-array impingement configurations [27] or narrow impingement cavities consisting of a single row of holes with developing crossflow [5]. In the present chart, however, only the first-row correlation from these studies is shown, corresponding to a confined cavity condition without crossflow, which is the closest analog to the current single-jet configuration.

Despite the geometric differences, the comparison remains meaningful at the area-averaged Nusselt number level. After Brinkman rescaling, air, N_2, Ar, and CO_2 collapse onto a common $\overline{\mathrm{Nu}}_D$–Re_D trend that is consistent with the first-row confined cavity correlations [5], with remaining offsets within experimental uncertainty. This agreement indicates that, once viscous dissipation effects are accounted for, the dominant scaling of the global heat transfer rate is governed primarily by jet momentum and confinement rather than by array-level interactions. Helium,

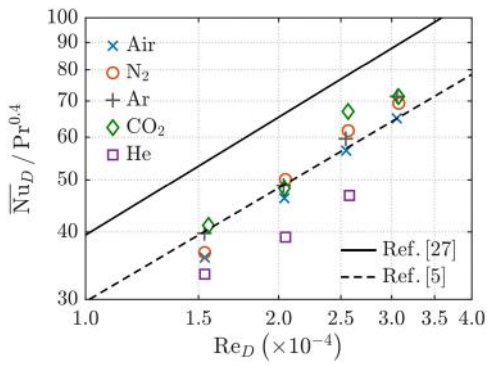

Fig. 11 Brinkman-rescaled Nusselt number, $\overline{\mathrm{Nu}}_D$, averaged over the whole impingement area versus Re_D for all tested gases. Dashed curves show representative first-row (no-crossflow) correlations for single-row narrow impingement cavity [5] and multi-array impingement configurations [27].

on the other hand, remains lower in $\overline{\mathrm{Nu}}_D$ even after Brinkman correction. Notably, the stagnation point heat transfer for helium is consistent with the corrected trend (see Fig. 10); however, helium exhibits systematically reduced heat transfer in the wall-jet region, which dominates the spatial average and therefore drives the lower $\overline{\mathrm{Nu}}_D$. Overall, Brinkman rescaling reconciles the global behavior of the moderate- and high-density gases, while Helium's reduced wall-jet performance persists and controls the area-averaged deviation.

6 Conclusions

This work experimentally assessed the validity and limitations of Reynolds–Prandtl similarity for fully confined single-exit round-jet impingement at $H/D = 1$ using five working gases (air, N_2, Ar, CO_2, He) over matched Reynolds numbers, $\mathrm{Re}_D = 15{,}000$–$30{,}000$. Spatially resolved heat-transfer coefficients were obtained using transient liquid crystal thermography with Duhamel superposition, while the nonideal driving temperature history was reconstructed using a two-time-scale input model with thermocouple response correction to ensure consistent thermal boundary conditions across gases.

At matched Reynolds number, normalized Stanton number fields demonstrated that the shape and spatial decay of the impingement footprint are measurably affected by gas properties. Air and N_2 produced nearly identical normalized distributions, providing a baseline reference. Relative to these, Ar and CO_2 exhibited systematically broader normalized footprints, indicating slower decay of heat transfer along the confined wall-jet region. In contrast, Helium produced a more compact normalized footprint with steeper downstream decay.

A Reynolds-only normalization with a common exponent $m = 0.7$ provided strong collapse across Reynolds numbers within each gas, isolating inter-gas property effects. Applying an additional Prandtl scaling with a common exponent ($\mathrm{Pr}^{0.4}$) collapsed the centerline distributions of air, N_2, Ar, and CO_2 over the stagnation and wall-jet regions, indicating that a single Prandtl exponent captures the dominant gas-to-gas variation among these heavier gases under the present confinement. Helium, however, remained a clear outlier under Reynolds–Prandtl scaling, suggesting that additional mechanisms become relevant when matching Reynolds number requires substantially higher jet velocities.

A Brinkman number analysis indicated that, under matched Reynolds number conditions, helium experiences significantly larger viscous dissipation/recovery temperature sensitivity due to its low density and the associated higher velocities. A simple Brinkman-based rescaling improved the collapse of helium data toward the heavier gas trends, supporting the interpretation that viscous heating effects contribute considerably to helium's deviation from Reynolds–Prandtl similarity.

Funding Data

- Technion Center for High-Speed Flight.
- The Minerva Research Center for Micro Turbine Powered Energy Systems (Max Planck Society Contract AZ5746940 764).

Conflict of Interest

There are no conflicts of interest.

Data Availability Statement

The datasets generated and supporting the findings of this article are obtainable from the corresponding author upon reasonable request.

Nomenclature

Symbols

h = convective heat transfer coefficient (W/m^2/K)
k = thermal conductivity of gas (W/m/K)
r = recovery factor (−)
t = time (s)
u = velocity component or mean velocity (m/s)
x = streamwise coordinate (m)
y = spanwise coordinate (m)
z = wall-normal coordinate (m)
$\dot{m}$ = mass flowrate (kg/s)
A = area (m^2)
D = jet/orifice diameter (m)
R = radial coordinate (m)
T = temperature (K or °C)
U = mean jet exit velocity (m/s)
c_p = specific heat at constant pressure (J/kg/K)
h_{sp} = stagnation point heat transfer coefficient (W/m/K)
k_{w} = thermal conductivity of wall (W/m/K)
t_{G} = green peak intensity time (s)
t_{R} = red peak intensity time (s)
t_0 = step onset time
$t_{0.99}$ = time at which $T_\infty(t)$ reaches 99% of the step (−)
z_{LC} = TLC indication depth (m)
A_{eff} = effective discharge area, $C_d A$ (m^2)
C_d = discharge coefficient (−)
D_h = hydraulic diameter (m)
T_{aw} = adiabatic wall (recovery) temperature (K or °C)
T_d = dynamic temperature, $T_t - T_s \approx U^2/(2c_p)$ (K)
T_g = bulk gas temperature (K or °C)
$T_{g,\mathrm{rec}}$ = reconstructed bulk gas temperature history (K or °C)
T_{LC} = TLC-indicated temperature, $T_{\mathrm{w}}(z_{\mathrm{LC}}, t)$ (K or °C)
T_m = measured thermocouple temperature (K or °C)
T_{s} = surface temperature, $T_{\mathrm{w}}(z = 0, t)$ (K or °C)
T_{w} = wall temperature (K or °C)
T_∞ = driving (mainstream) temperature at test section (K or °C)
$T_{\infty,0}$ = prestep driving temperature plateau (K or °C)
$T_{\infty,1}$ = poststep driving temperature plateau (K or °C)
q'' = surface heat flux (W/m^2)

Greek Symbols

α = thermal diffusivity of gas (m^2/s)
α_{w} = thermal diffusivity of wall, $k_{\mathrm{w}}/(\rho_{\mathrm{w}} c_{p,\mathrm{w}})$ (m^2/s)
β = (in Eq. (9)) weight of the fast exponential mode (−)
δ = thermocouple bead-to-wire diameter ratio (−)
δ_{bp} = black-paint thickness (m)
δ_{LC} = liquid crystal layer thickness (m)
ΔT = imposed thermal driving temperature difference (K)
ΔT_∞ = driving temperature step magnitude, $T_{\infty,1} - T_{\infty,0}$ (K)
θ = normalized temperature, $\theta = (T - T_{\infty,0})/(T_{\infty,1} - T_{\infty,0})$ (−)
μ = dynamic viscosity (Pa s)
ν = kinematic viscosity (m^2/s)
ρ = density of gas (kg/m^3)
ρ_{w} = density of wall (kg/m^3)
τ_{tc} = thermocouple time constant (s)
τ_1 = fast timescale of nonideal step model (s)
τ_2 = slow timescale of nonideal step model (s)
Φ = nondimensional wall response to an ideal step (−)

Dimensionless Groups

Br = Brinkman number, $\mu U^2/(k\Delta T) = \mathrm{Pr}\,\mathrm{Ec}$ (−)
Ec = Eckert number, $U^2/(c_p \Delta T)$ (−)
Ma = Mach number (−)
Nu = Nusselt number, hD/k (−)
Nu_{c} = Brinkman-corrected Nusselt number (Eq. (16)) (−)
$\mathrm{Nu}_{\mathrm{tc}}$ = thermocouple Nusselt number (Eq. (8)) (−)

Pe = Péclet number, Re Pr (−)
Pr = Prandtl number, $\nu/\alpha = \mu c_p/k$ (−)
Re_D = jet Reynolds number based on D, $\rho UD/\mu$ (−)
St = Stanton number, $h/(\rho U c_p)$ (−)

Subscripts and Superscripts

0 = initial/prestep value
1 = poststep value
d = dynamic (as in T_d)
m = measured (sensor output)
s = surface
t = total (stagnation)
w = wall
G = green TLC peak indicator
aw = adiabatic wall
bp = black paint
jet = jet exit condition
rec = reconstructed
sp = stagnation point
tc = thermocouple
LC = liquid crystal

Appendix A: Uncertainty Analysis

The uncertainty in heat transfer coefficient h is evaluated using standard first-order error propagation based on the sensitivity of h to independent input variables [49,50]. Linearization of the governing relation yields the sensitivity of the inferred heat transfer coefficient to each input parameter p_i:

$$\frac{\partial h}{\partial p_i} = -\frac{\partial y/\partial p_i}{\partial y/\partial h} \tag{A1}$$

where y represents the residual of the heat transfer model. Assuming the input uncertainties are uncorrelated, the variance of the heat transfer coefficient is obtained as follows:

$$\sigma_h^2 = \sum_i \left(\frac{\partial h}{\partial p_i}\right)^2 \sigma_{p_i}^2 = \sum_i \frac{\left(\frac{\partial y}{\partial p_i}\right)^2 \sigma_{p_i}^2}{\left(\frac{\partial y}{\partial h}\right)^2} \tag{A2}$$

The input parameters considered include the TLC peak green intensity temperature T_w, the initial temperature $T_{\infty,0}$, the driving gas temperature $T_{\infty,1}$, the TLC detection time t, the wall thermal conductivity k_w, thermal diffusivity α_w, and the TLC indication depth z_{LC}.

Figure 12(*a*) shows a representative map of heat transfer coefficient h, normalized by the stagnation point value ($h_{sp} = 184.7$ W/(m^{2}K)), for air as the working fluid, at $\mathrm{Re}_D = 25,000$. The distribution exhibits the characteristic impingement pattern, with a maximum at the stagnation point and a gradual decay along the wall-jet region, while remaining symmetric about the spanwise centerline ($y/D = 0$). This case is used as a reference example for the uncertainty analysis.

Using the sensitivity formulation above, the propagated uncertainty is evaluated pixelwise. Figure 12(*b*) shows the relative uncertainty σ_h/h at a 95% confidence level. The total uncertainty reaches its maximum at the stagnation region, where the inferred heat transfer coefficient is most sensitive to the TLC detection time. Away from the stagnation region, σ_h/h gradually decreases. The uncertainty field remains symmetric about the spanwise centerline ($y/D = 0$), consistent with the heat transfer coefficient pattern. Overall, σ_h/h remains within approximately 6–7.3% over the impingement surface.

To further quantify the relative importance of the different uncertainty sources, the contribution of each input parameter to the variance of h is evaluated for all experimental conditions and gases. Figure 12(*c*) summarizes the relative contributions of the individual uncertainty sources to the total variance σ_h^2 as a function of the nondimensional temperature $\theta = (T_w - T_{\infty,0})/(T_{\infty,1} - T_{\infty,0})$. The uncertainty associated with the wall thermophysical properties (k_w and α_w) dominates the uncertainty budget, contributing approximately 60–80% of the total variance. The uncertainty related to the TLC detection time t represents the second most significant contribution, accounting for 10–25%, whereas the contributions associated with the temperature ratio θ and the TLC indication depth z_{LC} are significantly smaller. The relative contributions exhibit weak dependence on the working gas, indicating that the uncertainty is primarily governed by the conduction model parameters rather than the flow conditions. Due to differences in heat transfer coefficients among the gases at matched Reynolds number, the temperature step was adjusted to ensure that the first TLC signal at the stagnation point appeared at approximately $t > 1.5$ s. Consequently, helium experiments, which exhibit higher heat transfer coefficients, correspond to larger values of θ, whereas gases with lower heat transfer coefficients (e.g., Ar and CO_2) populate the lower θ range.

For completeness, Table 3 summarizes representative input values, their associated uncertainties, and the relative contributions to the variance of the heat transfer coefficient at the stagnation point for the reference case (air, $\mathrm{Re}_D = 25,000$). The uncertainty associated with the wall thermophysical properties (k_w and α_w) dominates the uncertainty budget, accounting for $\approx 65\%$ of the total variance. The TLC detection time represents the second most significant contribution, contributing about 22%, while the uncertainties associated with the temperature measurements (T_w, T_g, T_0) and the TLC indication depth z_{LC} remain comparatively smaller. Combining all sources yields an overall uncertainty in the stagnation point heat transfer coefficient of approximately ±7.0% at a 95% confidence level.

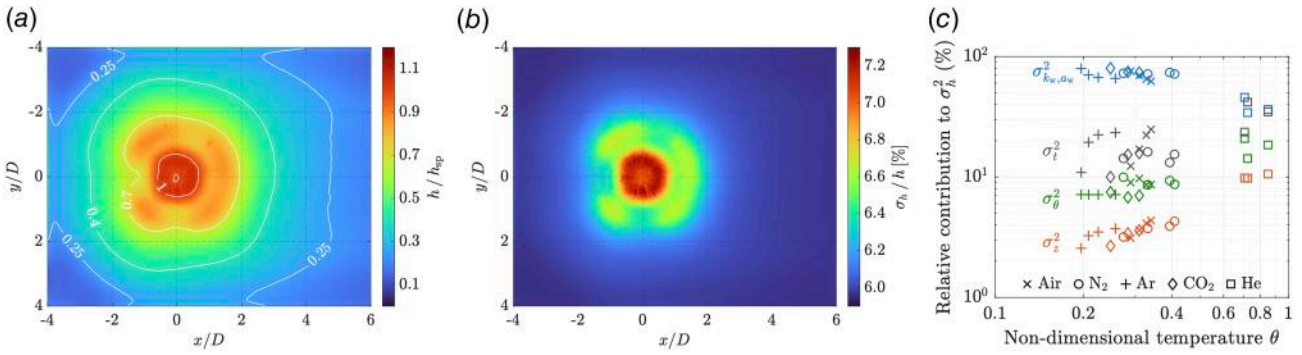

Fig. 12 (*a*) Representative heat transfer coefficient distribution h normalized with the stagnation point value ($h_{sp} = 184.7$/W m^{2}K), for air at $\mathrm{Re}_D = 25{,}000$. (*b*) Spatial distribution of the total uncertainty at a 95% confidence level for the same case. (*c*) Relative contributions of the different uncertainty sources to the variance σ_h^2 at the stagnation point for all experiments.

Table 3 Representative input parameters, associated uncertainties, and their relative contributions to the variance of the heat transfer coefficient at the stagnation point for the reference case (dry air, $Re_D = 25,000$)

Parameter	Unit	Value	Error (σ)	Contribution (%)
Initial temperature, $T_{\infty,0}$	°C	18.34	±0.14	2.1
Driving gas temperature, $T_{\infty,1}$	°C	56.59	±0.18	0.8
Maximum green intensity temperature, T_w	°C	30.86	±0.12	5.7
Peak TLC detection time, t_{LC}	s	1.62	±0.1	22.2
Wall thermal conductivity, k_w	W/(m K)	0.18	±5%	50.5
Wall thermal diffusivity, α_w ($\times 10^{-7}$)	m^2/s	1.029	±5%	14.6
TLC indication depth, z_{LC}	μm	25	±5	4.1
Heat transfer coefficient, h	W/(m^2K)	184.7	±13.0	≈7% (at 95% c)

Note: The table lists typical measured values, their standard uncertainties, and the resulting contribution to the total uncertainty.

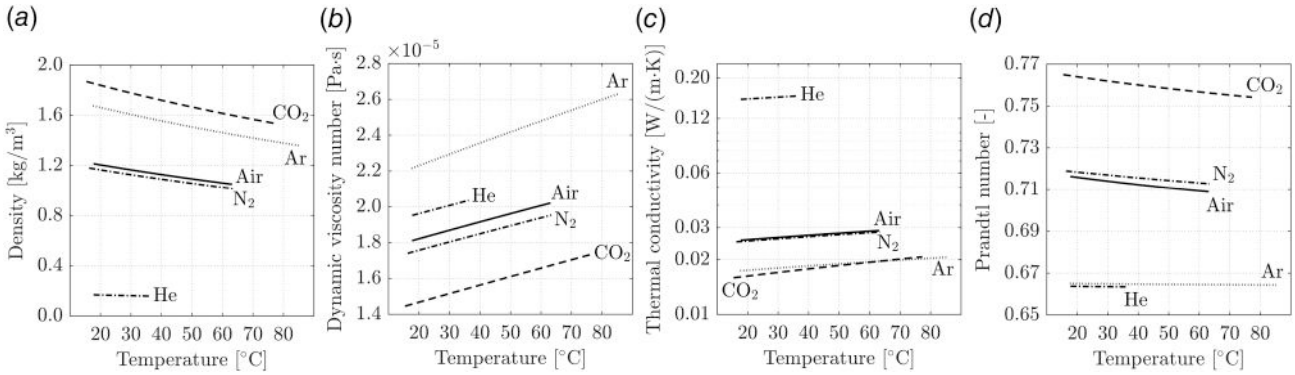

Fig. 13 Temperature dependence of the thermophysical properties of the working gases at 1 atm: (*a*) density, (*b*) dynamic viscosity, (*c*) thermal conductivity, and (*d*) Prandtl number. The temperature ranges correspond to the operating conditions of the experiments for each gas. The temperature step was adjusted for each gas to ensure the same first appearance time of the thermochromic liquid crystal response.

Appendix B: Thermophysical Properties of the Gases

Figure 13 shows the temperature dependence (at 1 atm) of the main thermophysical properties of the five working gases used in the experiments (air, N_2, Ar, CO_2, and He). These include the density ρ, dynamic viscosity μ, thermal conductivity k, and Prandtl number Pr. The properties are shown over the corresponding operating temperature ranges encountered in the experiments. These ranges differ between gases because the imposed temperature step was adjusted in each case to ensure the same first appearance time of the thermochromic liquid crystals (TLCs). Figure 13 highlights the main contrasts in gas properties across the experimental temperature ranges. In particular, helium exhibits a significantly lower density and a much higher thermal conductivity compared to the other gases, while CO_2 has the largest density and Prandtl number within the investigated temperature range. These variations affect the thermal transport characteristics of the impinging jet and provide additional context for interpreting the differences observed in the measured heat transfer distributions.

References

[1] Sellers, R. R., Soechting, F. O., Huber, F. W., and Auxier, T. A., "Cooled Blades for a Gas Turbine Engine," https://patents.google.com/patent/US5720431A/en, Accessed January 11, 2026.

[2] Fan, X., 2022, "Numerical Research of a New Vortex Double Wall Cooling Configuration for Gas Turbine Blade Leading Edge," Int. J. Heat Mass Transfer, **183**(Part A), p. 122048.

[3] Ma, L., Zhou, Z., Wang, J., and Yao, R., 2025, "Heat Transfer and Flow Characteristics of a Novel Double Wall Cooling Design Embedded by Primitive-Type Triply Periodic Minimal Surface Structures," Int. J. Heat Fluid Flow, **116**, p. 110005.

[4] Gillespie, D. R. H., Wang, Z., Ireland, P. T., and Kohler, S. T., 1998, "Full Surface Local Heat Transfer Coefficient Measurements in a Model of an Integrally Cast Impingement Cooling Geometry," ASME J. Turbomach., **120**(1), pp. 92–99.

[5] Terzis, A., Ott, P., von Wolfersdorf, J., Weigand, B., and Cochet, M., 2014, "Detailed Heat Transfer Distributions of Narrow Impingement Channels for Cast-In Turbine Airfoils," ASME J. Turbomach., **136**(9), p. 091011.

[6] Liang, J. C., 2013, "Turbine Stator Vane With Near Wall Integrated Micro Cooling Channels," U.S. Patent 8,414,263 B1, Apr. 9.

[7] Chambers, A. C., Gillespie, D. R. H., Ireland, P. T., and Dailey, G. M., 2005, "The Effect of Initial Cross Flow on the Cooling Performance of a Narrow Impingement Channel," J. Heat Transf., **127**(4), pp. 358–365.

[8] Chambers, A. C., Gillespie, D. R. H., Ireland, P. T., and Kingston, R., 2010, "Enhancement of Impingement Cooling in a High Cross Flow Channel Using Shaped Impingement Cooling Holes," ASME J. Turbomach., **132**(2), p. 021001.

[9] Choo, K. S., and Kim, S. J., 2010, "Comparison of Thermal Characteristics of Confined and Unconfined Impinging Jets," Int. J. Heat Mass Transfer, **53**(15–16), pp. 3366–3371.

[10] Caggese, O., Gnaegi, G., Hannema, G., Terzis, A., and Ott, P., 2013, "Experimental and Numerical Investigation of a Fully Confined Impingement Round Jet," Int. J. Heat Mass Transfer, **65**, pp. 873–882.

[11] Baughn, J. W., and Shimizu, S., 1989, "Heat Transfer Measurements From a Surface With Uniform Heat Flux and an Impinging Jet," ASME J. Heat Transfer, **111**(4), pp. 1096–1098.

[12] Ricklick, M., Kapat, J. S., and Heidmann, J., 2010, "Sidewall Effects on Heat Transfer Coefficient in a Narrow Impingement Channel," J. Thermophys. Heat Transfer, **24**(1), pp. 123–132.

[13] Nagathan, V., Khalifa, M., Angadi, B. M., Adimurthy, M., and Katti, V., 2025, "Confinement Size Dependency of Flow Structures and Thermal Characteristics in Turbulent Impinging Air Jet on a Flat Target Surface," Int. Commun. Heat Mass Transfer, **169**, p. 109683.

[14] Terzis, A., Wagner, G., von Wolfersdorf, J., Ott, P., and Weigand, B., 2014, "Hole Staggering Effect on the Cooling Performance of Narrow Impingement Channels Using the Transient Liquid Crystal Technique," ASME J. Heat Transfer, **136**(7), p. 071701.

[15] Lamont, J. A., Ekkad, S. V., and Alvin, M. A., 2012, "Effects of Rotation on Heat Transfer for a Single Row Jet Impingement Array With Crossflow," ASME J. Heat Transfer, **134**(8), p. 082202.

[16] Singh, P., and Ekkad, S. V., 2018, "Detailed Heat Transfer Measurements of Jet Impingement on Dimpled Target Surface Under Rotation," ASME J. Therm. Sci. Eng. Appl., **10**(3), p. 031006.

[17] Forster, M., and Weigand, B., 2021, "Experimental and Numerical Investigation of Jet Impingement Cooling Onto a Concave Leading Edge of a Generic Gas Turbine Blade," Int. J. Therm. Sci., **164**, p. 106862.

[18] Bergamin, G., Moura, L. M., and Mendes, N., 2026, "Experimental Evaluation of the Heat Transfer From Submerged and Confined Circular Jets on Curved Surfaces," Int. J. Therm. Sci., **222**, p. 110523.
[19] Stoakes, P., and Ekkad, S., 2011, "Optimized Impingement Configurations for Double Wall Cooling Applications," ASME Turbo Expo, Paper No. GT2011-46143, pp. 1535–1543.
[20] Llucià, S., Terzis, A., Ott, P., and Cochet, M., 2015, "Heat Transfer Characteristics of High Crossflow Impingement Channels: Effect of Number of Holes," Proc. Inst. Mech. Eng., Part A: J. Power Energy, **229**(5), pp. 560–568.
[21] Terzis, A., Skourides, C., Ott, P., von Wolfersdorf, J., and Weigand, B., 2016, "Aerothermal Investigation of a Single Row Divergent Narrow Impingement Channel by Particle Image Velocimetry and Liquid Crystal Thermography," ASME J. Turbomach., **138**(5), p. 051003.
[22] Madhavan, S., Ramakrishnan, K. R., Singh, P., and Ekkad, S., 2019, "Jet Impingement Heat Transfer Enhancement by U-Shaped Crossflow Diverters," ASME J. Therm. Sci. Eng. Appl., **12**(4), p. 041005.
[23] Uysal, U., Li, P.-W., Chyu, M. K., and Cunha, F. J., 2006, "Heat Transfer on Internal Surfaces of a Duct Subjected to Impingement of a Jet Array With Varying Jet Hole-Size and Spacing," ASME J. Turbomach., **128**(1), pp. 158–165.
[24] Terzis, A., Ott, P., Cochet, M., von Wolfersdorf, J., and Weigand, B., 2015, "Effect of Varying Jet Diameter on the Heat Transfer Distributions of Narrow Impingement Channels," ASME J. Turbomach., **137**(2), p. 021004.
[25] Gao, L., Ekkad, S. V., and Bunker, R. S., 2005, "Impingement Heat Transfer Part I: Linearly Stretched Arrays of Holes," J. Thermophys. Heat Transfer, **19**(1), pp. 57–65.
[26] Shi, Y., Ray, M. B., and Mujumdar, A. S., 2002, "Effects of Prandtl Number on Impinging Jet Heat Transfer Under a Semi-Confined Turbulent Slot Jet," Int. Commun. Heat Mass Transfer, **29**(7), pp. 929–938.
[27] Florschuetz, L. W., Truman, C. R., and Metzger, D. E., 1981, "Streamwise Flow and Heat Transfer Distributions for Jet Array Impingement With Crossflow," ASME J. Heat Transfer, **103**(2), pp. 337–342.
[28] Li, C.-Y., and Garimella, S. V., 2001, "Prandtl-Number Effects and Generalized Correlations for Confined and Submerged Jet Impingement," Int. J. Heat Mass Transfer, **44**(18), pp. 3471–3480.
[29] Ma, C. F., 2002, "Impingement Heat Transfer With Meso-Scale Fluid Jets," International Heat Transfer Conference 12, Grenoble, France, Aug. 18–23, Begellhouse, p. 3310.
[30] Sun, H., Ma, C. F., and Tian, Y. Q., 1997, "Local Convective Heat Transfer From Small Heaters to Impinging Submerged Axisymmetric Jets of Seven Coolants With Prandtl Number Ranging From 0.7 to 348," J. Therm. Sci., **6**(4), pp. 286–297.
[31] Sun, H., Ma, C. F., and Chen, Y. C., 1998, "Prandtl Number Dependence of Impingement Heat Transfer With Circular Free-Surface Liquid Jets," Int. J. Heat Mass Transfer, **41**(10), pp. 1360–1363.
[32] Sun, H., and Ma, C. F., 1998, "Effect of Variable Fluid Properties on Impingement Heat Transfer With Submerged Circular Jets," Int. J. Heat Mass Transfer, **41**(10), pp. 1363–1366.
[33] Yuan, Z. X., Chen, Y. Y., Jiang, J. G., and Ma, C. F., 2006, "Swirling Effect of Jet Impingement on Heat Transfer From a Flat Surface to CO_2 Stream," Exp. Therm. Fluid Sci., **31**(1), pp. 55–60.
[34] Rahman, M. M., Bula, A. J., and Leland, J. E., 1999, "Conjugate Heat Transfer During Free Jet Impingement of a High Prandtl Number Fluid," Numer. Heat Transf., B: Fundam., **36**(2), pp. 139–162.
[35] Lemmon, E. W., Bell, I. H., Huber, M. L., and McLinden, M. O., 2023, "Thermophysical Properties of Fluid Systems," NIST Chemistry WebBook.
[36] Kingsley-Rowe, J. R., Lock, G. D., and Michael Owen, J., 2005, "Transient Heat Transfer Measurements Using Thermochromic Liquid Crystal: Lateral-Conduction Error," Int. J. Heat Fluid Flow, **26**(2), pp. 256–263.
[37] Hüning, M., 2010, "Comparison of Discharge Coefficient Measurements and Correlations for Orifices With Cross-Flow and Rotation," ASME J. Turbomach., **132**(3), p. 031017.
[38] Kwak, J. S., 2008, "Comparison of Analytical and Superposition Solutions of the Transient Liquid Crystal Technique," J. Thermophys. Heat Transfer, **22**(2), pp. 290–295.
[39] Terzis, A., Wolfersdorf, J. V., Weigand, B., and Ott, P., 2012, "Thermocouple Thermal Inertia Effects on Impingement Heat Transfer Experiments Using the Transient Liquid Crystal Technique," Meas. Sci. Technol., **23**(11), p. 115303.
[40] Huang, Q., Yue, L., Li, X., and Wang, P., 2024, "A Correlation to Calculate Time Constant of Thermocouples," Appl. Therm. Eng., **246**, p. 122920.
[41] Terzis, A., Bontitsopoulos, S., Ott, P., von Wolfersdorf, J., and Kalfas, A. I., 2016, "Improved Accuracy in Jet Impingement Heat Transfer Experiments Considering the Layer Thicknesses of a Triple Thermochromic Liquid Crystal Coating," ASME J. Turbomach., **138**(2), p. 021003.
[42] Schulz, S., Brack, S., Terzis, A., Wolfersdorf, J. V., and Ott, P., 2016, "On the Effects of Coating Thickness in Transient Heat Transfer Experiments Using Thermochromic Liquid Crystals," Exp. Therm. Fluid Sci., **70**, pp. 196–207.
[43] Kim, B. G., Yu, M. S., Cho, Y. I., and Cho, H. H., 2002, "Distributions of Recovery Temperature on Flat Plate by Underexpanded Supersonic Impinging Jet," J. Thermophys. Heat Transfer, **16**(3), pp. 425–431.
[44] Goldstein, R. J., Behbahani, A. I., and Heppelmann, K. K., 1986, "Streamwise Distribution of the Recovery Factor and the Local Heat Transfer Coefficient to an Impinging Circular Air Jet," Int. J. Heat Mass Transfer, **29**(8), pp. 1227–1235.
[45] Goldstein, R. J., Sobolik, K. A., and Seol, W. S., 1990, "Effect of Entrainment on the Heat Transfer to a Heated Circular Air Jet Impinging on a Flat Surface," ASME J. Heat Transfer, **112**(3), pp. 608–611.
[46] Schmid, J., Gaffuri, M., Terzis, A., Ott, P., and von Wolfersdorf, J., 2021, "Transient Liquid Crystal Thermography Using a Time Varying Surface Heat Flux," Int. J. Heat Mass Transfer, **179**, p. 121718.
[47] Lee, J. and Lee, S.-J., 1999, "Stagnation Region Heat Transfer of a Turbulent Axisymmetric Jet Impingement," Exp. Heat Transfer, **12**(2), pp. 137–156.
[48] Hollworth, B. R., and Berry, R. D., 1978, "Heat Transfer From Arrays of Impinging Jets With Large Jet-to-Jet Spacing," ASME J. Heat Transfer, **100**(2), pp. 352–357.
[49] Moffat, R. J., 1988, "Describing the Uncertainties in Experimental Results," Exp. Therm. Fluid. Sci., **1**(1), pp. 3–17.
[50] Coleman, H. W., and Glenn Steele, W., Jr., 2009, *Experimentation, Validation, and Uncertainty Analysis for Engineers*, 4th ed., John Wiley & Sons, Inc., Hoboken, NJ.